Negative linear compressibility and unusual dynamic behavior of NaB_3

Xin-Ling He,[1] Shu-Ning Pan,[2] Yue Chen,[3,4] Xiao-Ji Weng,[1] Zifan Wang,[1] Dongli Yu,[5] Xiao Dong,[1,*] Jian Sun,[2,†] Yongjun Tian,[5] and Xiang-Feng Zhou[1,5,‡]

[1]*Key Laboratory of Weak-Light Nonlinear Photonics and School of Physics, Nankai University, Tianjin 300071, China*

[2]*National Laboratory of Solid State Microstructures, School of Physics and Collaborative Innovation Center of Advanced Microstructures, Nanjing University, Nanjing 210093, China*

[3]*Department of Mechanical Engineering, The University of Hong Kong, Pokfulam Road, Hong Kong SAR, China*

[4]*HKU Zhejiang Institute of Research and Innovation, 1623 Dayuan Road, Lin An 311305, China*

[5]*Center for High Pressure Science, State Key Laboratory of Metastable Materials Science and Technology, School of Science, Yanshan University, Qinhuangdao 066004, China*

(Received 28 September 2020; revised 27 January 2021; accepted 22 February 2021; published 2 March 2021)

First-principles calculations reveal that sodium boride (NaB_3) undergoes a phase transition from a tetragonal $P4/mbm$ phase to an orthorhombic $Pbam$ phase at ∼16 GPa, accompanied by a counterintuitive lattice expansion along the crystallographic a axis. This unusual compression behavior is identified as negative linear compressibility (NLC), which is dominantly attributed to the symmetry breaking of the boron framework. Meanwhile, the $P4/mbm$ and $Pbam$ phases form superionic conductors after undergoing a peculiar swap state at high temperature. Specifically, under "warm" conditions the Na cation pairs exhibit a rare local exchange (rotation) behavior, which may be originated from the asymmetric energy barriers of different diffusion paths. The study of the NaB_3 compound sheds light on a material with a combination of NLC and ion transportation at extreme conditions.

DOI: 10.1103/PhysRevMaterials.5.035002

I. INTRODUCTION

High pressure (HP) and high temperature (HT) can significantly alter both the crystal structure and electronic properties of a material without creating any external impurities, leading to a tremendous amount of discovery of new compounds and unusual properties. For instance, most matter contracts in all directions under hydrostatic pressure, whereas very few materials expand along one direction coupled to the volume reduction due to its anisotropy, which is defined as negative linear compressibility (NLC) [1–3]. Several NLC materials were previously reported in dense inorganic oxides and fluorides, as well as a few complex organics [4–11]. On the basis of this anomalous mechanical property, the NLC materials have important applications in the design of pressure sensors, actuators, artificial muscles, and optical fibers with high shock resistance [2,12–16].

Another example relates to superionic compounds, also denoted as fast ion conductors or solid electrolytes, whose structures usually contain rigid frameworks with open channels along which ions can migrate [17–19]. Superionic materials featured by a liquidlike conductivity within the fixed crystalline frameworks have long attracted enormous attention for batteries, fuel cells, thermoelectrics, and other energy applications, e.g., $Li_{10}GeP_2S_{12}$, LiAlSO, and Cu_2Se [20–22]. Furthermore, a few common materials such as ice and ammonia exhibit a superionic state at HPHT conditions, which even improves our knowledge of the middle ice layers of Neptune and Uranus [17,18].

In this paper, we surprisingly found sodium boride (NaB_3) had a temperature-induced swap state beside superionicity and NLC simultaneously, providing a representative example to better understand the relationship between structures and properties. Especially for Na-B compounds, only a few compounds are precisely determined with regard to their compositions and structures [23–25]. The previously predicted phase of $I2_12_12_1$-Na_2B_{30} with an unprecedented open-framework boron sublattice is helpful to resolve the debate on the ground-state structure of sodium borides, whereas the $Imma$-Na_2B_{30} structure was a topological nodal line semimetal with a potentially superior electronic transport property [26].

II. METHOD

Structure searches were performed utilizing the *ab initio* evolutionary algorithm USPEX [27,28] for NaB_3 with up to six formula units (f.u.) per supercell under various pressures. The structure relaxations and electronic properties were carried out using density functional theory (DFT) within the Perdew-Burke-Ernzerhof (PBE) parametrization of the generalized gradient approximation (GGA) exchange-correlation functional [29] as implemented in the VASP code [30]. The $2s^22p^63s^1$ and $2s^22p^1$ electrons were treated as valences for Na and B, respectively. A plane-wave basis set

*xiao.dong@nankai.edu.cn
†jiansun@nju.edu.cn
‡xfzhou@nankai.edu.cn

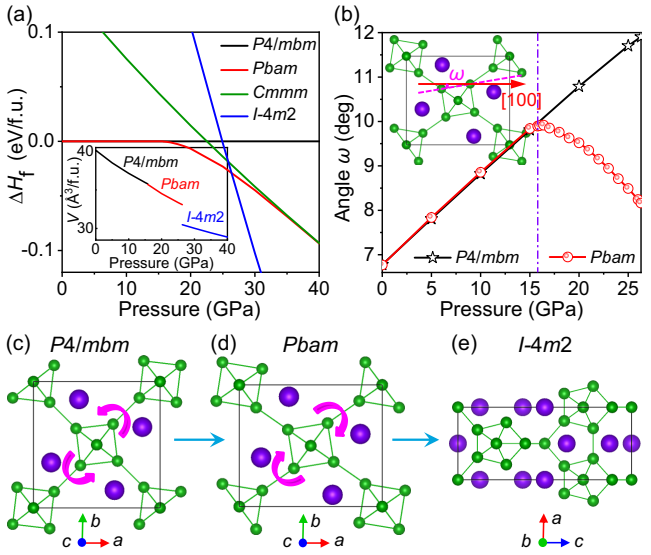

FIG. 1. (a) The enthalpy difference of NaB_3 compounds as a function of pressure with respect to the $P4/mbm$ phase. The inset shows the pressure-volume relations. (b) The variation of the angle ω as a function of pressure. The inset shows the angle ω between the orientation of the centered B_6 octahedral and [100] direction. (c)–(e) Schematic views of the structural evolutions of the NaB_3 system during compression. The rotation direction of the B_6 octahedral is labeled by magenta arrows as increasing pressure. Purple and green balls represent the Na and B atoms, respectively.

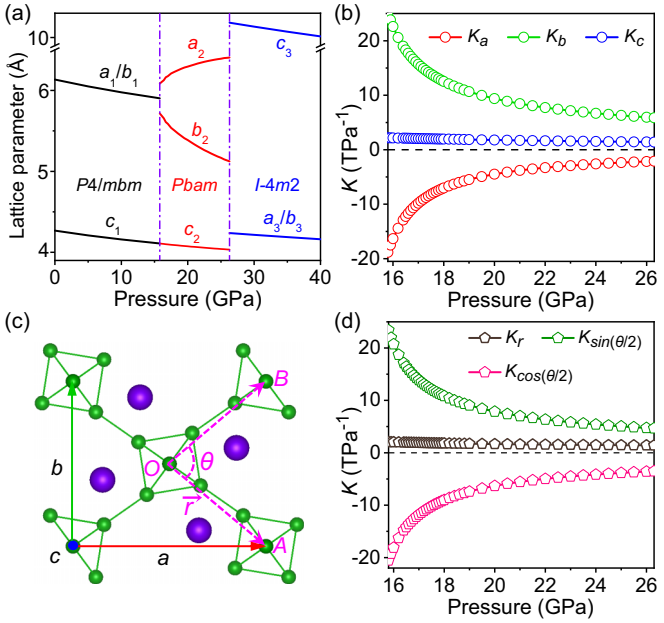

FIG. 2. (a) The lattice parameters of various NaB_3 phases as a function of pressure. (b) The compressibility of the principal axes for the *Pbam* phase as a function of pressure. (c) The structural projection of the *Pbam* phase along the [001] direction, where the letters of *A*, *O*, and *B* are the centers of the B_6 octahedra. The coordinates of *A*, *O*, and *B* are (1, 0, 1/2), (1/2, 1/2, 1/2), and (1, 1, 1/2), respectively. (d) Evolution of compressibility for the distance *r* (*O*-*A* or *O*-*B*), $\sin(\theta/2)$ and $\cos(\theta/2)$ within the pressure range of 15.8–26.3 GPa.

with an energy cutoff of 850 eV and uniform Γ-centered *k*-point grids with a resolution of $2\pi \times 0.02$ Å^{-1} were used. The structures were fully optimized until the maximum energy and force were less than 10^{-8} eV and 0.001 eV/Å, respectively. Band structures were also calculated by using the Heyd-Scuseria-Ernzerhof (HSE06) functional [31]. *Ab initio* molecular dynamics (AIMD) simulations [32] were carried out using a $2 \times 2 \times 3$ supercell for the $P4/mbm$ and *Pbam* phases, and a $2 \times 2 \times 2$ supercell for the $I\bar{4}m2$ phase. A Nosé-Hoover thermostat was adopted to perform the *NVT* simulations with a temperature range of 500–4500 K lasting for 10 ps with a time step of 1 fs. The statistical information of each atomic trajectory was extracted from the last 5 ps. To confirm the system's stability, some trajectory calculations were extended to 40 ps. The phonon dispersion curve of $P4/mbm$ NaB_3 was performed using the finite displacement method ($2 \times 2 \times 2$ supercell) with the PHONOPY code [33]. In addition, the energy barrier was calculated by the climbing-image nudged elastic band (CI-NEB) method [34].

III. RESULTS AND DISCUSSION

The phase diagram and physical properties of NaB_3 compounds are systematically investigated. Since the enthalpy of formation of $P4/mbm$-NaB_3 is negative (Fig. S1) referring to the enthalpies of the bcc-Na and α-boron structure or any isochemical mixture of Na-B compounds [35], first-principles calculations reveal that the $P4/mbm$-NaB_3 system is stable above ~0.4 GPa and may be quenchable to ambient pressure because there are no imaginary phonon frequencies in the whole Brillouin zone (Fig. S2) [35]. The enthalpy-pressure curves show that NaB_3 undergoes a reversible phase transition from a tetragonal $P4/mbm$ phase to an orthorhombic *Pbam* phase at ~16 GPa. The *Pbam* symmetry is the subgroup of $P4/mbm$ symmetry with an index of two, and the fourfold rotation symmetry is broken (mainly attributed to the rotation of the B_6 octahedron) as pressure is increased. Moreover, no chemical bonds break during the phase transition, leading to the gradual variation of volume and the reversible phase transition. Then *Pbam*-NaB_3 undergoes an irreversible phase transition to another tetragonal $I\bar{4}m2$ phase at ~26 GPa [Fig. 1(a)]. The phase transition from a $P4/mbm$ to *Pbam* structure is accompanied by a negligible volume change, indicative of the second-order phase transition, while there is a 7.87% volume collapse for the phase transition from the *Pbam* to $I\bar{4}m2$ structure, characteristic of a first-order phase transition [the inset of Fig. 1(a)]. These results are different from the reported phase transition from $P4/mbm$ to *Cmmm*-NaB_3 [36,37], and the *Cmmm* structure is higher in enthalpy than the proposed phases at the studied pressure range.

The crystal structures of the $P4/mbm$ and *Pbam* phases are plotted in Figs. 1(c) and 1(d). They are composed of interstitial Na atoms and different boron frameworks, that is, a B_6-octahedral network for the $P4/mbm$ and *Pbam* structures, whereas the dominant B_8-dodecahedral network for the $I\bar{4}m2$ phase [Fig. 1(e)]. As shown in Fig. 1(b), the angle (ω) between the orientation of the centered B_6 octahedra (marked by the magenta dotted line) and the [100] direction is employed to explore the underlying mechanism for the reversible phase transition. Clearly, the angle ω in the $P4/mbm$ phase

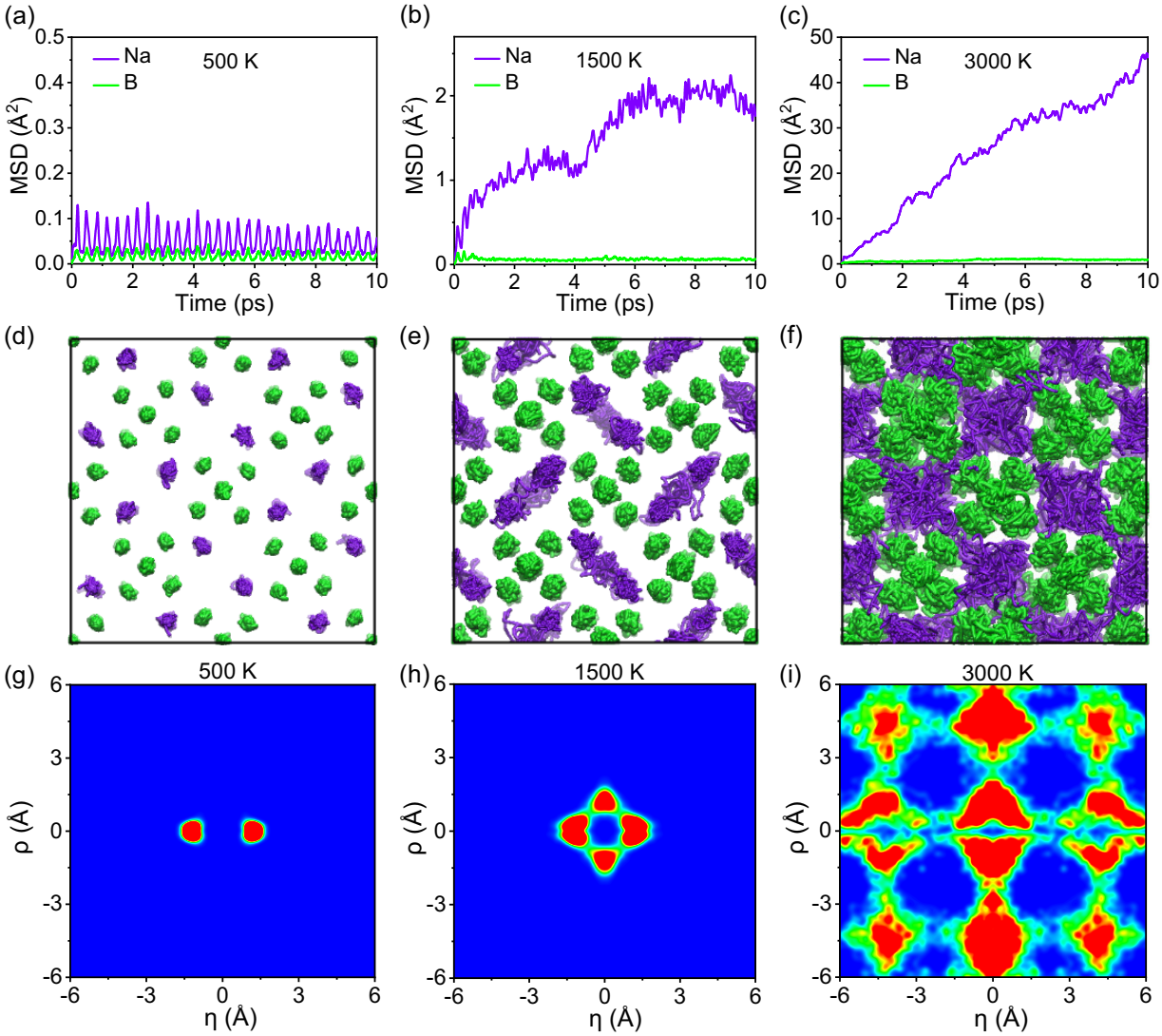

FIG. 3. (a)–(c) The MSDs from AIMD simulations for the Na and B atoms in the $P4/mbm$ phase at ambient pressure and different temperatures. (d)–(f) The projection of atomic trajectories along the [001] direction in the $P4/mbm$ phase from the last 5 ps run representing the solid phase (500 K), the swap phase (1500 K), and the superionic phase (3000 K). (g)–(i) The probability of the presence of Na atoms at 500, 1500, and 3000 K.

is linearly increased as a function of pressure owing to the counterclockwise rotation of the centered B_6 octahedron. In contrast, it abruptly decreases in a parabolic shape from 15.8 to 26.3 GPa because of the opposite rotation behavior of the B_6 octahedron in the *Pbam* phase. As further increasing pressure above 26 GPa, the B_6 octahedra are destroyed and transform into distorted B_8 dodecahedra and interstitial B atoms, resulting in the formation of the $I\bar{4}m2$ phase. The lattice parameters of NaB_3 under selected pressures are listed in Table S1 [35]. Moreover, band structure calculations show that all predicted NaB_3 compounds are semiconductors. Most strikingly, the DFT band gap of the *Pbam* structure is increased as a function of pressure and different from other NaB_3 phases (Fig. S3) [35], which is partially originated from the NLC effect.

Unexpectedly, the phase transition from the $P4/mbm$ to *Pbam* phase is quite different from those second-order phase transitions [38–41], because it is accompanied by the emergence of an anomalous lattice expansion along the crystallographic *a* axis (belonging to the proper ferroelastic transitions [5]) whereas normal lattice contractions along the *b* and *c* axes within a pressure range of ∼16–26 GPa [Fig. 2(a)]. The compressibility of a material is generally defined as the relative change rate of dimensions with respect to pressure at a constant temperature, $K_i = -(1/i)(\partial i/\partial p)_T$, where *i* can be assigned as the volume (V), area (A), and linear (l) compressibility, respectively [2]. The compressibility coefficients of the principal axes for the *Pbam* phase (equivalent to crystallographic axes in an orthorhombic structure), computed by the PASCal program in the pressure range from 15.8 to 26.3 GPa [42], are $K_a = -6.65$ TPa^{-1}, $K_b = 12.10$ TPa^{-1}, and $K_c = 1.94$ TPa^{-1}, respectively. The variation of the compressibility as a function of pressure is plotted in Fig. 2(b). It shows NLC along the *a* axis while there is a positive line compressibility (PLC) along the *b* and *c* axes. The mechanism of NLC can be rationalized by its special geometrical configuration.

For *Pbam*-NaB_3, the distance r and angle θ with respect to the three nearest centers of the neighboring B_6 octahedra are illustrated in Fig. 2(c). The lattice constants a and b have a relationship with r and θ as follows: $a = 2r\cos(\theta/2)$, $b = 2r\sin(\theta/2)$; $K_a = -(1/a)(\partial a/\partial p) = K_r + K_{\cos(\theta/2)}$, $K_b = -(1/b)(\partial b/\partial p) = K_r + K_{\sin(\theta/2)}$. It is evident that the values of r and θ ($\theta < 90^\circ$) decrease as pressure increases from 15.8 to 26.3 GPa (Fig. S4) [35], resulting in a positive K_r, a positive $K_{\sin(\theta/2)}$, and a negative $K_{\cos(\theta/2)}$. As shown in Fig. 2(d), since K_r is much smaller than $K_{\sin(\theta/2)}$ and $K_{\cos(\theta/2)}$, the compressibility along the a axis (b axis) is dominantly determined by $K_{\cos(\theta/2)}$ ($K_{\sin(\theta/2)}$) in the *Pbam* phase. Compared with the compression behavior of the $P4/mbm$ phase, the pressure-induced opposite rotation of B_6 octahedra in the *Pbam* phase significantly enhances the change rate of θ above 16 GPa, which guarantees a small K_r and a large K_θ value, leading to NLC accordingly.

To further examine the thermodynamic stability of the $P4/mbm$ phase, we performed AIMD simulations at ambient pressure and the temperature range of 500–4500 K by analyzing a combination of mean square displacements (MSDs) and atomic trajectories. At 500 K, the oscillations of Na and B atoms with respect to their equilibrium positions indicate that the $P4/mbm$ structure is stable, hence it maintains a solid phase without any migrations [Figs. 3(a) and 3(d)]. At 1500 K, the MSDs of Na atoms demonstrate a steplike increase in several picoseconds, indicating a special displacement during this stage [Fig. 3(b)]. Upon a more detailed study of the atomic trajectories, the local exchange among Na atoms is observed and designated as an intermediate state, as shown in Fig. 3(e) and the Supplemental Material [35]. The Na cation pairs composed of the nearest-neighboring Na atoms rotate ~90° nearly parallel to the (110) or ($\bar{1}$10) plane, and then rotate to the initial positions or exchanged positions. This isolated rotation behavior is similar to that of molecular crystals, such as the low-temperature phase of H_2 in hexagonal-close-packed (hcp) form [43]. However, unlike H_2 molecules, there is a strong electrostatic repulsion between Na cations instead of covalent bonds. Therefore, the intermediate state of NaB_3 may be termed as a "swap" phase, which will be further discussed in the later section. At 3000 K, the Na atoms vibrate strongly and migrate freely within a fixed open-framework boron structure, resulting in persistently ascendant MSDs with a diffusion constant of approximately 0.69×10^{-8} $m^2\,s^{-1}$. All these indicate the $P4/mbm$ phase turns into a superionic conductor [Figs. 3(c) and 3(f)]. When temperature is increased beyond 3500 K, the $P4/mbm$ phase melts.

Figures 3(g)–3(i) plot the probability density maps of Na atoms [44], showing the diffusive feature of Na atoms in the $P4/mbm$ phase. The coordinates were first built, with the center $\mathbf{r}_c = [\boldsymbol{\mu}_i(0) + \boldsymbol{\mu}_j(0)]/2 = \boldsymbol{\mu}_i(t)$-$\boldsymbol{\mu}'_i(t)$ defined as the midpoint of the Na-Na vector, where i, j are the atomic numbers of the nearest-neighboring Na atoms, and $\boldsymbol{\mu}_i(t)$ represents the position vector of the ith atom at the moment of t. We defined a parameter of $\hat{\boldsymbol{\eta}}$ as the nearest Na-Na vector and the coordinate $\eta = \boldsymbol{\mu}'_i(t) \cdot \hat{\boldsymbol{\eta}}$ of a given atom i. The other coordinate ρ is defined as $\rho = \sqrt{||\boldsymbol{\mu}'_i(t)||^2 - \eta^2} = ||\boldsymbol{\mu}'_i(t) - \eta\hat{\boldsymbol{\eta}}||$. At 500 K, the $P4/mbm$ phase retains the solid state [Fig. 3(g)]. When temperature further increases to 1500 K, the diffusive

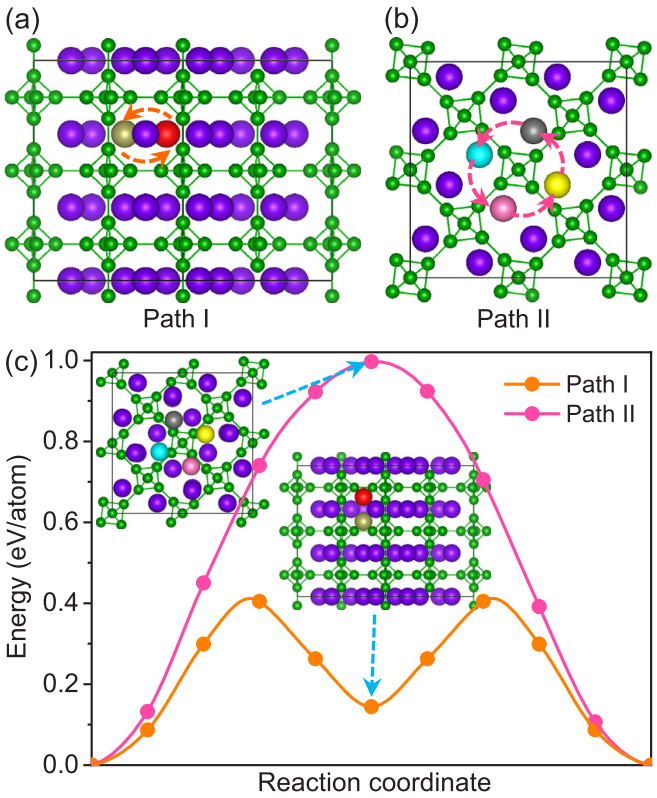

FIG. 4. (a), (b) Potential Na diffusion paths, where local exchanges for the Na pairs (path I) and interpaired Na atoms (path II). The color balls represent the exchanged Na atoms. (c) Calculated energy barriers of the $P4/mbm$ phase with different Na diffusion paths. The insets show the structural illustrations of the saddle point at path I and path II.

trajectories of the Na atoms involving the rotation behavior of Na pairs can be characterized by a diamond shape with two diagonal lines of ~2.43 Å (the distance of Na pairs in the initial position) and ~2.39 Å (the distance of Na pairs rotating ~90° relative to its initial positions) [Fig. 3(h)]. All Na pairs have a similar distance of approximately 2.14–2.43 Å with fixed mass centers, implying a swap state. To reveal the likely mechanism of this particular state, the potential migration paths of Na atoms are studied by the CI-NEB method, where the initial and final states are identical but with different diffusion paths [Figs. 4(a) and 4(b)]. The results show the energy barrier of the swap state (0.39 eV/atom) is lower than that of interpaired Na atoms (0.99 eV/atom) [Fig. 4(c)], indicating that the asymmetric energy barrier may be dominantly responsible for the origin of the swap state. As temperature reaches 3000 K, Na atoms diffuse freely within the fixed boron frameworks, entering a superionic state [Fig. 3(i)]. According to the multiple transition states discussed above, we expanded the pressure range up to 60 GPa to explore the phase diagram of NaB_3. The systematical AIMD simulations at HPHT show that the *Pbam* phase also exhibits a solid-swap-superionic-fluid phase transition similar to the $P4/mbm$ phase (Fig. S5) [35], while the $I\bar{4}m2$ phase transforms directly from solid to fluid above 4000 K (Figs. S6 and 5) [35].

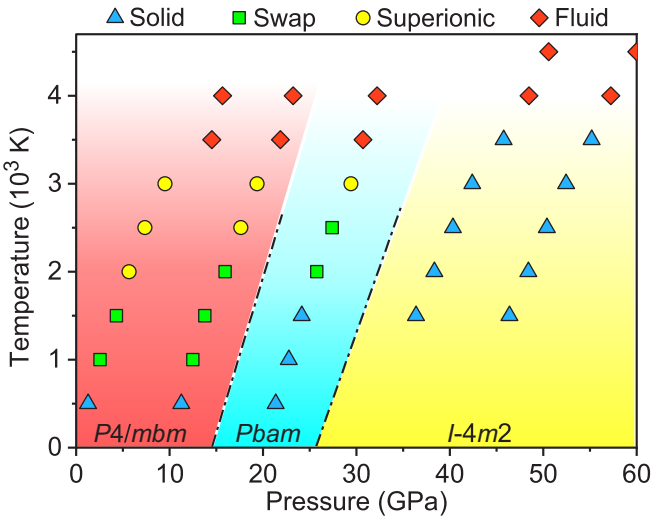

FIG. 5. The phase diagram of the NaB_3 system. The symbols of blue triangles, green squares, yellow circles, and jacinth diamonds represent solid, swap, superionic, and fluid states, respectively. The data points marked by color symbols in red, cyan, and yellow shaded areas relate to $P4/mbm$, $Pbam$, and $I\bar{4}m2$ phases, respectively.

IV. CONCLUSION

In summary, the phase diagram and compression behavior of NaB_3 have been systematically studied from first principles. Under high pressure, a solid-solid phase transition originating from the symmetry breaking of the boron framework results in a striking NLC effect. At high temperature, a phase transition sequence of a solid-swap-superionic-fluid state is identified by the AIMD simulations. Interestingly, different from the normal solid-superionic phase transition, the particular swap state attributed to the local diffusion of Na pairs may give a deeper insight into the understanding of ion transportation.

ACKNOWLEDGMENTS

This work was supported by the National Science Foundation of China (Grants No. 11874224, No. 52025026, No. 52090020, No. 51772263, and No. 21803033), the Tianjin Science Foundation for Distinguished Young Scholars (Grant No. 17JCJQJC44400), and Young Elite Scientists Sponsorship Program by Tianjin (No. TJSQNTJ-2018-18). X.D. and X.-F.Z. thank the computing resources of Tianhe II and the support of the Chinese National Supercomputer Center in Guangzhou.

[1] R. Gatt and J. N. Grima, Phys. Status Solidi RRL **2**, 236 (2008).
[2] R. H. Baughman, S. Stafström, C. Cui, and S. O. Dantas, Science **279**, 1522 (1998).
[3] A. D. Fortes, E. Suard, and K. S. Knight, Science **331**, 742 (2011).
[4] L. Ming, M. H. Manghnani, T. Matsui, and J. C. Jamieson, Phys. Earth Planet. Inter. **23**, 276 (1980).
[5] A. B. Cairns and A. L. Goodwin, Phys. Chem. Chem. Phys. **17**, 20449 (2015).
[6] Q. Zeng, K. Wang, and B. Zou, J. Am. Chem. Soc. **139**, 15648 (2017).
[7] Q. Zeng, K. Wang, Y. Qiao, X. Li, and B. Zou, J. Phys. Chem. Lett. **8**, 1436 (2017).
[8] Q. Zeng, K. Wang, and B. Zou, ACS Mater. Lett. **2**, 291 (2020).
[9] W. Cai and A. Katrusiak, Nat. Commun. **5**, 4337 (2014).
[10] W. Cai, J. He, W. Li, and A. J. Katrusiak, J. Mater. Chem. C **2**, 6471 (2014).
[11] A. B. Cairns, J. Catafesta, C. Levelut, J. Rouquette, A. van der Lee, L. Peters, A. L. Thompson, V. Dmitriev, J. Haines, and A. L. Goodwin, Nat. Mater. **12**, 212 (2013).
[12] A. L. Goodwin, D. A. Keen, and M. G. Tucker, Proc. Natl. Acad. Sci. USA **105**, 18708 (2008).
[13] X. Jiang, S. Luo, L. Kang, P. Gong, W. Yao, H. Huang, W. Li, R. Huang, W. Wang, Y. Li, X. Li, X. Wu, P. Lu, L. Li, C. Chen, and Z. Lin, Adv. Mater. **27**, 4851 (2015).
[14] A. E. Aliev, J. Oh, M. E. Kozlov, A. A. Kuznetsov, S. Fang, A. F. Fonseca, R. Ovalle, M. D. Lima, M. H. Haque, Y. N. Gartstein, M. Zhang, A. A. Zakhidov, and R. H. Baughman, Science **323**, 1575 (2009).
[15] R. H. Baughman, Nature (London) **425**, 667 (2003).
[16] K. E. Evans and A. Alderson, Adv. Mater. **12**, 617 (2000).
[17] P. Demontis, R. LeSar, and M. L. Klein, Phys. Rev. Lett. **60**, 2284 (1988).
[18] C. Cavazzoni, G. L. Chiarotti, S. Scandolo, E. Tosatti, M. Bernasconi, and M. Parrinello, Science **283**, 44 (1999).
[19] C. Liu, H. Gao, A. Hermann, Y. Wang, M. Miao, C. J. Pickard, R. J. Needs, H.-T. Wang, D. Xing, and J. Sun, Phys. Rev. X **10**, 021007 (2020).
[20] N. Kamaya, K. Homma, Y. Yamakawa, M. Hirayama, R. Kanno, M. Yonemura, T. Kamiyama, Y. Kato, S. Hama, K. Kawamoto, and A. Mitsui, Nat. Mater. **10**, 682 (2011).
[21] X. Wang, R. Xiao, H. Li, and L. Chen, Phys. Rev. Lett. **118**, 195901 (2017).
[22] H. Liu, X. Shi, F. Xu, L. Zhang, W. Zhang, L. Chen, Q. Li, C. Uher, T. Day, and G. J. Snyder, Nat. Mater. **11**, 422 (2012).
[23] R. Naslain and J. S. Kasper, J. Solid State Chem **1**, 150 (1970).
[24] B. Albert, K. Hofmann, C. Fild, H. Eckert, M. Schleifer, and R. Grurhn, Chem. Eur. J. **6**, 2531 (2000).
[25] B. Albert, Angew. Chem., Int. Ed. **37**, 1117 (1998).
[26] X.-L. He, X. Dong, Q. S. Wu, Z. Zhao, Q. Zhu, A. R. Oganov, Y. Tian, D. Yu, X.-F. Zhou, and H.-T. Wang, Phys. Rev. B **97**, 100102(R) (2018).
[27] A. R. Oganov and C. W. Glass, J. Chem. Phys. **124**, 244704 (2006).
[28] O. Lyakhov, A. R. Oganov, H. T. Stokes, and Q. Zhu, Comput. Phys. Commun. **184**, 1172 (2013).
[29] J. P. Perdew, K. Burke, and M. Ernzerhof, Phys. Rev. Lett. **77**, 3865 (1996).
[30] G. Kresse and J. Furthmüller, Comput. Mater. Sci. **6**, 15 (1996).
[31] J. Heyd, G. E. Scuseria, and M. Ernzerhof, J. Chem. Phys. **124**, 219906 (2006).

[32] R. Car and M. Parrinello, Phys. Rev. Lett. **55**, 2471 (1985).
[33] A. Togo and I. Tanaka, Scr. Mater. **108**, 1 (2015).
[34] G. Henkelman, B. P. Uberuaga, and H. Jónsson, J. Chem. Phys. **113**, 9901 (2000).
[35] See Supplemental Material at http://link.aps.org/supplemental/10.1103/PhysRevMaterials.5.035002 for crystal structural parameters and electronic properties of the related NaB_3 phases, as well as the local exchange behavior of Na cation pairs at 1500 K.
[36] Y. Zhong, C.-H. Hu, D.-h. Wang, and H.-Y. Zhou, J. Alloys Compd. **731**, 323 (2018).
[37] S. Zhang, X. Du, J. Lin, A. Bergara, X. Chen, X. Liu, X. Zhang, and G. Yang, Phys. Rev. B **101**, 174507 (2020).
[38] G. Li, Y. Li, M. Zhang, Y. Ma, Y. Ma. Y. Han, and C. Gao, RSC Adv. **4**, 42523 (2014).
[39] R. Vilaplana, S. G. Parra, A. Jorge-Montero, P. Rodríguez-Hernández, A. Munoz, D. Errandonea, A. Segura, and F. J. Manjón, Inorg. Chem. **57**, 8241 (2018).
[40] E. Bandiello, D. Errandonea, S. Ferrari, J. Pellicer-Porres, D. Martínez-García, S. N. Achary, A. K. Tyagi, and C. Popescu, Inorg. Chem. **58**, 4480 (2019).
[41] C. Ji, B. Li, W. Liu, J. S. Smith, A. Majumdar, W. Luo, R. Ahuja, J. Shu, J. Wang, S. Sinogeikin, Y. Meng, V. B. Prakapenka, E. Greenberg, R. Xu, X. Huang, W. Yang, G. Shen, W. L. Mao, and H.-K. Mao, Nature (London) **573**, 558 (2019).
[42] M. J. Cliffe and A. L. Goodwin, J. Appl. Crystallogr. **45**, 1321 (2012).
[43] H.-k. Mao and R. J. Hemley, Rev. Mod. Phys. **66**, 671 (1994).
[44] D. Corradini, F.-X. Coudert, and R. Vuilleumier, Nat. Chem. **8**, 454 (2016).